



A systematic analysis of Cu-based membrane-electrode assemblies for CO₂ reduction through multiphysics simulation

Journal:	<i>Energy & Environmental Science</i>
Manuscript ID	EE-ART-05-2020-001604.R2
Article Type:	Paper
Date Submitted by the Author:	13-Aug-2020
Complete List of Authors:	Weng, Lien-Chun; University of California Berkeley, Bell, Alexis; University of California, Chemical and Biomolecular Engineering Weber, Adam; Lawrence Berkeley National Laboratory, Energy Technologies Area

A systematic analysis of Cu-based membrane-electrode assemblies for CO₂ reduction through multiphysics simulation

Lien-Chun Weng,^{1,2} Alexis T. Bell,^{*1,2} and Adam Z. Weber^{*1}

¹Joint Center for Artificial Photosynthesis, LBNL, Berkeley CA 94720

²Dept. Chemical and Biomolecular Engineering, UC Berkeley, Berkeley CA 94720

Abstract

Copper-based membrane-electrode assemblies (Cu-MEAs) hold promise for increasing the energy efficiency for the electrochemical reduction of CO₂ to C₂₊ products, while maintaining high current densities. However, fundamental understanding of Cu-MEAs is still limited compared to the wealth of knowledge available for aqueous electrolyte Cu systems. Physics-based modeling can assist in the transfer of knowledge from aqueous to vapor-fed systems by deconvoluting the impacts of various physical processes and accelerating the optimization of Cu-MEAs. Here, we simulate Cu-MEA performance and describe how the change in cell architecture leads to changes in cell performance and optimization. Our results reveal nonuniformity of product distribution in the catalyst layer and explore the catalyst-layer properties as a design parameter for increasing the energy efficiency of C₂₊ product formation. We discuss multiphase flow and water-management issues and show how membrane properties, specifically the electro-osmotic coefficient, affects the efficacy of feeding liquid water to hydrate the membrane. Finally, we explore tradeoffs associated with operating Cu-MEAs at 350 K in order to increase the supply of water and the preferential formation of products with higher activation energies (typically C₂₊ products).

Introduction

Electrochemical CO₂ reduction (CO₂R) has gained significant attention in recent years as a means for reducing atmospheric CO₂ levels and storing excess renewable energy.^{1, 2} Technoeconomic analysis emphasizes the need to operate CO₂R at current densities above 100 mA/cm² for industrial viability,³ and gas-diffusion electrodes (GDEs) play an important role in achieving such high rates.^{4, 5} By decreasing CO₂ diffusion length to the catalyst, GDEs minimize not only CO₂ mass-transfer resistances, but also the unfavorable CO₂/OH⁻ interactions, allowing CO₂R to occur in much more alkaline environments, suppressing the unfavorable hydrogen evolution reaction (HER).^{4, 6, 7} The operation of Cu-based GDEs under alkaline conditions has also been shown to attain higher faradaic efficiencies (FEs) for C₂₊ products, which are desirable because of their high energy densities and market value.⁷⁻¹⁰ Finally, membrane-electrode assemblies (MEAs) have proven to be effective in minimizing cell ohmic losses and circumventing issues associated with having the GDE in direct contact with an aqueous electrolyte, such as electrode flooding and salt precipitation.^{7, 11, 12} Therefore, Cu-MEAs provide an opportunity to achieve high energy efficiencies (EEs) for the desired products while maintaining a high production rate.

Recent work has demonstrated promising progress towards achieving high activity and stability for both CO₂R and CO reduction (COR) using Cu-MEAs. Ripatti et al. have reported a current density greater than 100 mA/cm² at 2.4 V maintained for over 24 h, with a 24% EE for COR to ethylene and acetate.⁸ Sullivan et al. have achieved up to 70% FE towards C₂₊ products from CO reduction.⁹ For CO₂R, Gabardo et al. have demonstrated stable operation for 100 h at over 100 mA/cm² with 40% C₂H₄ FE and 23% EE towards C₂₊ products.¹³ While these numbers are encouraging, a large design space for Cu-MEAs remains to be explored. Optimization of the various design and operating parameters, such as cell geometry, operating temperature etc., can be guided by physics-based simulation. However, only limited work has been reported on the simulation of a Cu-MEA system for CO₂R. Gabardo et al. calculated the distribution of voltage losses in their experimental device,¹³ and Sullivan et al. presented a model for water transport in order to analyze the level of hydration in their experimental Cu-MEA setup.⁹ Both studies included portions of relevant physics – the first focused on electrochemistry, the second, on water management – but a comprehensive model that includes the effects of electrode kinetics, mass and energy transport is still lacking. Furthermore, neither of the previous studies investigated the impact of changes in cell properties or operating conditions on cell performance expressed in terms of product distribution and voltage utilization.

In this study, we discuss the performance and limitation of Cu-MEAs deduced from simulations conducted with a multiphysics model built upon our previous work.¹¹ The model was updated to include the following: (1) the kinetics of CO₂R on Cu for the formation of H₂, CO, HCOOH, CH₄, C₂H₄, C₂H₅OH, and C₃H₇OH; (2) the liquid phase water pressure and multiphase interactions including evaporation/condensation, capillary effects, etc.; (3) the transport of an additional anionic species, formate, through the membrane. We break down the overpotentials required to drive various processes and explore ways to minimize them. Our analysis shows how catalyst layer properties, membrane properties, and operating conditions impact cell performance and product distribution through the complex interplay and tradeoffs of various physical processes.

Theory

The multiphysics model developed in this work is built upon previous models developed for CO₂R electrolyzers^{6, 11} and H₂ fuel cells.¹⁴⁻¹⁶ **Figure 1** shows a schematic and the dimensions of the base-case Cu-MEA system examined in this study. It is a one-dimensional model with five domains: anode/cathode diffusion medium (aDM/cDM), anode/cathode catalyst layer (aCL/cCL), and an anion-exchange membrane (AEM). The porous CLs consist of catalyst particles and ionomer (an ion-conducting polymer). We assume that the catalyst particles are coated with a 10 nm thick ionomer thin film that provides a pathway for ions to transport from the CL to the AEM. While ionomer thin films have been shown to have properties that differ from those of bulk membranes of the same material,¹⁷⁻²⁰ the properties of AEM thin films are not firmly established; therefore, we assume the ionomer thin films to have the same properties as those of the membrane. Reactants are fed to gas channels next to the DM. The feed flowrates are assumed to be high enough such that the composition in the gas channel remains constant.

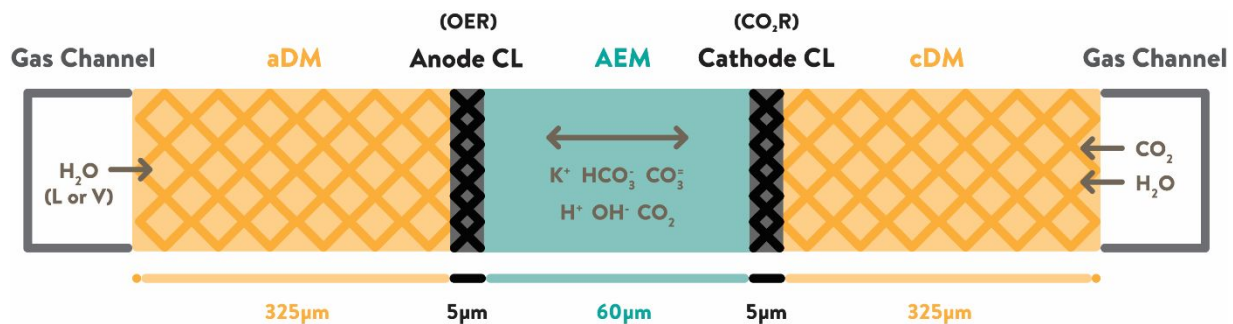


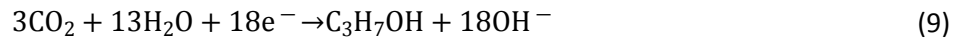
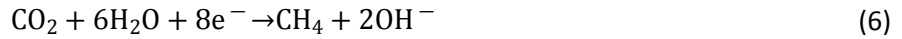
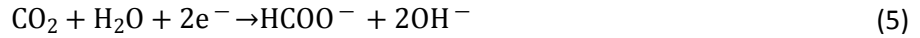
Figure 1 Schematic of the Cu-MEA system.

Charge transfer kinetics

The oxygen evolution reaction (OER) is catalyzed by IrO₂ at the anode:



The hydrogen evolution reaction (HER) and CO₂R reactions occur at the Cu cathode. The following cathodic reactions are considered,



The partial current density for product k is described by the Tafel equation,

$$i_k = i_{o,k} \prod_j \left(\frac{c_j}{c_j^{\text{ref}}} \right)^{\gamma_{j,k}} \cdot \exp \left(- \frac{\alpha_{c,k} F}{RT} \eta_k \right) \quad (10)$$

where η_k is the overpotential, defined as the deviation of the electrode potential from the equilibrium potential after Nernstian correction,

$$\eta_k = (\phi_S - \phi_L) - \left(U_k^o - \frac{2.303RT}{F} \text{pH} \right) \quad (11)$$

The electric potential, ϕ_S , and the electrolyte potential, ϕ_L , are determined by solving Equations (12), (13), (17), and (23), discussed below. The kinetic parameters used in our simulation were extracted from experimental measurements on roughened Cu²¹ after correcting for concentration polarization effects in the experiments with an 80- μm boundary-layer model (discussed further in the SI).²² We should note that the exact kinetics in the CL environment are not necessarily the same as that in the aqueous solution due to different ion concentrations, types, etc.;^{23, 24} but devoid of any data, we use these kinetics to see how

the MEA device operates. We choose to use the kinetics for CO₂R on a roughened Cu (rather than a polished one) for the balance of our analysis because we consider such a surface to be a better representation of Cu-MEAs based on their similarities to fuel cell systems.^{25, 26} This choice is also supported by recent experimental studies of Cu-MEAs, which exhibit a low FE for CH₄, a characteristic of rough Cu surfaces,^{8, 9, 13} and likely a result of increased grain boundary density.²⁷⁻²⁹ Additionally, the six cathode products observed on the roughened Cu accounts for six of the seven major products detected in the Cu-MEA setup by Gabardo et al.¹³ In the last section, an alternate set of self-consistent kinetics³⁰ is used to further show the generality of the trends observed. The exchange current density, $i_{o,k}$, anodic/cathodic transfer coefficient, $\alpha_{a/c,k}$, activity dependence, $\prod_j a_j^{\gamma_{j,k}}$, and standard electrode potential, U_k^0 , are summarized in **Table 1**. The activity of water, a_w , is defined in Equation (22), and the activity of all other species is defined as $a_{j \neq w} = \frac{c_j}{c^{\text{ref}}}$ referenced to $c^{\text{ref}} = 1 \text{ M}$.

Table 1 Rate parameters for charge transfer reactions

	U_k^0 (V)	$i_{o,k}$ (mA cm ⁻²)	$\alpha_{a/c,k}$	$\prod_j a_j^{y_{j,k}}$	Ref.
<i>OER on IrO₂</i>					31-34
O₂ (acid)	1.23	$1.2 \times 10^{-8} \exp\left(-\frac{0.01[\text{eV}]\text{pH}}{k_B T}\right)$	1.5	$a_w^{1.6}$	
O₂ (base)		$1.6 \times 10^{-6} \exp\left(-\frac{0.01[\text{eV}]\text{pH}}{k_B T}\right)$		a_{OH^-}	
<i>HER & CO₂R on roughened Cu</i>					21, 35
H₂	0	$1.0 \times 10^{-2} \exp\left(-\frac{0.01[\text{eV}]\text{pH}}{k_B T}\right)$	0.28	a_w^2	
CO	-0.11	2.6	0.17	$a_w \left(\frac{[\text{CO}_2]}{1 \text{ M}}\right)^{1.50}$	
HCOO⁻	-0.02	2.2×10^{-1}	0.37	$a_w \left(\frac{[\text{CO}_2]}{1 \text{ M}}\right)^{2.00}$	
C₂H₄	0.07	1.9×10^{-6}	0.67	$a_w^3 \left(\frac{[\text{CO}_2]}{1 \text{ M}}\right)^{1.36}$	
C₂H₅OH	0.08	1.2×10^{-8}	0.74	$a_w^3 \left(\frac{[\text{CO}_2]}{1 \text{ M}}\right)^{0.96}$	
C₃H₇OH	0.09	4.9×10^{-9}	0.75	$a_w^4 \left(\frac{[\text{CO}_2]}{1 \text{ M}}\right)^{0.96}$	

The solid-phase electric potential, ϕ_s , is determined by solving charge conservation,

$$\nabla \cdot \mathbf{i}_s = - \sum_k a_{s,k} i_k \quad (12)$$

and Ohm's law,

$$\mathbf{i}_s = - \sigma_{s,m}^{\text{eff}} \nabla \phi_s \quad (13)$$

where \mathbf{i}_s is the current density in the solid phase, $\sigma_{s,m}^{\text{eff}}$ is the effective electronic conductivity of medium m and $a_{s,k}$ is the specific active surface area (surface area per unit volume) for reaction k . For reactions

with gas-phase reactants, such as CO₂R, accumulation of liquid water in the CL can block access to active sites. This is accounted for by including a correction to the intrinsic specific surface area, a_s^o , as follows,

$$a_{s,k} = (1 - S_{CL})a_s^o \quad (14)$$

where S_{CL} is the saturation level of the CL, describing the fraction of pores in the GDE filled with liquid water. This differs from our previous model where $a_{s,k}$ was corrected with the liquid volume fraction instead of the gas volume fraction due to the differences in CL composition.⁶ The CL in the previous model did not include an ionomer component, so liquid electrolyte was necessary to provide an ionic pathway in the CL. Whereas the CL in the current model consists of an ionomer layer covering the catalyst particles, providing an ionic pathway. *In both cases, too much liquid in the CL pores becomes an impediment to gas transport to the catalyst surface.* S_{CL} is determined from the capillary pressure ($p_C = p_L - p_G$), and its relationship is plotted in **Figure S2a**.

Gas and liquid water transport in the DM and CL

The gas and liquid pressures in the porous media (DM and CL) are calculated via mass conservation,

$$\nabla \cdot \rho_p \mathbf{u}_p = Q_p \quad (15)$$

and Darcy's law,

$$\mathbf{u}_p = - \frac{\psi_{m,p}^{\text{eff}}}{\mu_p} \nabla p_p \quad (16)$$

where \mathbf{u}_p is the mass-averaged velocity field of phase p ; $\psi_{m,p}^{\text{eff}}$ is the effective permeability of phase p in medium m ; ρ_p and μ_p are the fluid density and viscosity, respectively; Q is the mass source term, discussed below.

The gas phase contains CO₂, H₂O, H₂, CO, CH₄, C₂H₄, O₂, and N₂; the mole fractions are calculated from mole balance,

$$\nabla \cdot \mathbf{N}_i = R_{B,i} + R_{CT,i} + R_{PT,i} \quad (17)$$

where $R_{B,i}$, $R_{CT,i}$, and $R_{PT,i}$, describe the molar source terms of species i due to charge transfer reactions, bulk homogeneous reactions, and phase-transfer reactions, respectively. The molar flux, \mathbf{N}_i , is determined from the mass flux,

$$\mathbf{N}_i = \frac{1}{M_i} \left(-\rho_G D_i^{\text{eff}} \nabla \omega_i - \rho_G D_i^{\text{eff}} \omega_i \frac{\nabla M_A}{M_A} + \rho_i \mathbf{u}_G \right) \quad (18)$$

where ρ_G is the gaseous mixture density; ω_i , M_i , D_i^{eff} , is the mass fraction, molecular weight, and effective diffusion coefficient of species i , respectively; $M_A = \left(\sum_i \frac{\omega_i}{M_i} \right)^{-1}$ is the average molecular weight of the mixture. Additionally,

$$\sum_i x_i = 1 \quad (19)$$

where the mole fraction $x_i = \frac{\omega_i M_A}{M_i}$.

Species concentration and the ionic potential in the ionomer and the membrane

Concentrations profiles for five charged species (OH^- , HCO_3^- , $\text{CO}_3^{=}$, H^+ , HCOO^-) and three neutral species (H_2O , CO_2 , HCOOH) in the membrane and the ionomer are determined by simulation. Gaseous species N_2 , O_2 , H_2 , CO , CH_4 , C_2H_4 are neglected due to their low solubilities in the ionomer.³⁶⁻³⁸ $\text{C}_2\text{H}_5\text{OH}$ (EtOH) and $\text{C}_3\text{H}_7\text{OH}$ (PrOH) can leave the system in both liquid and vapor phases; products in liquid phase can be collected in the cathode outlet, or transport across the membrane and collected in the anode outlet.¹³ Although the presence of these alcohols can affect ionomer properties,³⁹⁻⁴¹ there is limited data on their interactions with AEMs. Consequently, we do not account for these effects in this study. For simplicity, we assume that EtOH and PrOH leave the system rapidly and, therefore, we do not include their transport in the model. Finally, formic acid is included in the model as it participates in the acid-base reaction with HCOO^- , but it is also assumed to transport out of the system rapidly.

The molar flux of water, \mathbf{N}_w , occurs via diffusion and electro-osmosis,

$$\mathbf{N}_w = -\alpha_w^{\text{eff,M}} \nabla \mu_w + \sum_j \xi_j^{\text{eff,M}} \mathbf{N}_j \quad (20)$$

where $\alpha_w^{\text{eff,M}}$ is the effective water transport coefficient, $\xi_j^{\text{eff,M}}$ is the effective electro-osmotic coefficient (EOC) of species j . However, there is a paucity of measured data for $\xi_j^{\text{eff,M}}$ for the various ionic species present in our system;⁴² therefore, we use an overall EOC, $\xi_A^{\text{eff,M}}$, determined as

$$\sum_j \xi_j^{\text{eff,M}} \mathbf{N}_j = -\xi_A^{\text{eff,M}} \frac{\mathbf{i}_L}{F} \quad (21)$$

Since anions carry the net charge in an AEM, the electro-osmotic flux is in the opposite direction to the current density in the membrane/ionomer phase, \mathbf{i}_L , hence the negative sign. The derivation for $\xi_A^{\text{eff},M}$ is provided in Equations S4~S6.

The chemical potential of water, μ_w , is defined as

$$\mu_w = RT \ln a_w + \overline{V}_{w,L}(p_{L,M} - p^{\text{ref}}) \quad (22)$$

where $a_w = p_V/p_w^{\text{vap}}$ is the activity of water vapor referenced to its vapor pressure, $\overline{V}_{w,L}$ is the molar volume of liquid water, $p_{L,M}$ is the pressure of liquid water in the membrane, and p^{ref} is a reference pressure of 1 atm.

The molar flux of all other species, $\mathbf{N}_{j \neq w}$, is described by the Nernst-Planck equation,

$$\mathbf{N}_{j \neq w} = -D_j^{\text{eff}} \nabla c_j + \frac{z_j F}{RT} D_j^{\text{eff}} c_j \nabla \phi_L \quad (23)$$

where D_j^{eff} , c_j , z_j are the effective diffusivity, concentration, and charge of species j , respectively. The second term describes the migration flux of charged species and does not apply to CO_2 . Additionally, electroneutrality is needed to solve for the electrolyte ionic potential,

$$\sum_j z_j c_j = 0 \quad (24)$$

It should be noted that the Nernst-Planck equation assumes dilute-solution theory and our system is not necessarily dilute under all conditions. However, there is insufficient data available to completely describe all the frictional interactions that would need to be accounted for in our model. Recently, Crothers et al. have introduced a novel method based on thermodynamic⁴³ and transport⁴⁴ theories to predict these frictional forces in a cation-exchange membrane environment. However, these methodologies have not been generalized for AEMs and rely on certain data that has yet to be obtained; hence, it remains an active area of research and is not incorporated in this model.

Heat transfer

The temperature profile in the system is obtained by solving the energy conservation equation,

$$\nabla \cdot (-k_{T,m} \nabla T) = \Omega_{CT} + \Omega_B + \Omega_{PT} + \Omega_j \quad (25)$$

where $k_{T,m}$ is the thermal conductivity of medium m ; Ω_{CT} , Ω_B , Ω_{PT} , Ω_j are the heat generation terms from charge transfer reactions, bulk buffer reactions, phase transfer, and joule heating, respectively.

Bulk reactions and phase-transfer reactions

The source terms appearing in the conservation equations (15), (17), and (25) are obtained from appropriate rate expressions. The volumetric molar source term due to homogeneous reactions, $R_{B,j}$, occurs in the ionomer and the membrane, and accounts for the following reactions:



where k_n and k_{-n} are the rate constants for the forward and reverse directions of homogeneous reaction n and K_n is the equilibrium constant. $R_{B,j}$ can then be calculated as follows,

$$R_{B,j} = \sum_n s_{j,n} c^{\text{ref}} \left(k_n \prod_{s_{j,n} < 0} a_j^{-s_{j,n}} - \frac{k_n}{K_n} \prod_{s_{j,n} > 0} a_j^{s_{j,n}} \right) \quad (32)$$

where $s_{j,n}$ is the stoichiometric coefficient (negative for reactants and positive for products) for species j in reaction n .

The source terms for charge transfer reactions, $R_{CT,j}$, occur only in the CL domains, and is a function of the partial current densities for reactions (1)-(9),

$$R_{CT,j} = - \sum_k \frac{s_{j,k} a_{s,k} i_k}{n_k F} \quad (33)$$

where n_k is the number of electrons transferred in reaction k , i_k and $a_{s,k}$ is described in Equations (10) and (14), respectively.

$R_{PT,j,p}$ describes the rate of mass transfer of species CO_2 , HCOOH , and H_2O between gas|ionomer, liquid|ionomer, and gas|liquid phases in the direction towards phase p . For CO_2 and HCOOH , $R_{PT,j,l}$ occurs only in the CL, and describes the rate of mass transfer to the ionomer

$$R_{PT,j,l} = a_s k_{MT,j} (c_j^{\text{eq}} - c_j) \quad (34)$$

where $k_{MT,j}$ is the mass transfer coefficient, c_j^{eq} is the concentration of species j in equilibrium with its concentration external to the ionomer. For HCOOH, we assume it transports out of the CL rapidly so we set $c_{HCOOH}^{eq} = 0$; for CO₂, $c_{CO_2}^{eq} = p_G y_{CO_2} H_{CO_2}$, the product of the gas phase pressure, the mole fraction of CO₂ in the gas phase, and Henry's constant for CO₂. For H₂O in the ionomer,

$$R_{PT,w,I} = a_s k_{MT,V} \left(\frac{RH}{100} - a_w \right) + \frac{a_s k_{MT,L}}{RT} (p_L - p_{L,M}) \quad (35)$$

which includes phase transfer of both vapor H₂O and liquid H₂O to the ionomer. Here, $k_{MT,V}$ and $k_{MT,L}$ are the mass transfer coefficients for vapor water set to 0.06 mol/m²·s, and liquid water set to 10⁴ m/s, respectively.^{15, 45} RH is the relative humidity of the gas phase, defined as $RH = \frac{p_G y_0}{p_0^{sat}} \times 100\%$. For H₂O in the gas phase,

$$R_{PT,w,G} = -a_s k_{MT,V} \left(\frac{RH}{100} - a_w \right) - k'_{MT} (RH - 100\%) \left[H_0 \left(\frac{p_L}{p^{ref}} \right) + H_0 (RH - 100\%) \right] \quad (36)$$

where the first term describes mass transfer between vapor water and the ionomer in the CL, and the second term describes water evaporation/condensation in both the CL and the DM. An arbitrarily large mass transfer coefficient, $k'_{MT} = 10^7$ mol/m³·s, and a Heaviside step function, $H_0(x)$, ensure that $RH = 100\%$ when liquid water is present ($p_L > 0$), and that RH does not exceed 100%. Similarly, for H₂O in the liquid phase,

$$R_{PT,w,L} = -a_s \frac{k_{MT,L}}{RT} (p_L - p_{L,M}) + k'_{MT} (RH - 100\%) \left[H_0 \left(\frac{p_L}{p^{ref}} \right) + H_0 (RH - 100\%) \right] \quad (37)$$

where the first term describes mass transfer between liquid water and the ionomer in the CL, and the second term describes water evaporation/condensation.

The volumetric mass source terms, Q , in the overall mass balance (Equation (15)) need to be treated separately for gas and liquid phases. Q_G includes the phase transfer of gaseous CO₂ and H₂O to the ionomer, as well as gaseous species produced from the charge transfer reactions, O₂, H₂, CO, CH₄, C₂H₄,

$$Q_G = -M_{CO_2} R_{PT,CO_2,I} + M_w R_{PT,w,G} + \sum_{i \neq CO_2, H_2O, N_2} M_i R_{CT,i} \quad (38)$$

Since H₂O is the only component in the liquid phase, Q_L only includes one term,

$$Q_L = M_w R_{PT,w,L} \quad (39)$$

Heat generation from charge transfer reactions include both irreversible and reversible terms,

$$\Omega_{CT} = \sum_k (i_k \eta_k + i_k \Pi_k) \quad (40)$$

where Π_k is the Peltier coefficient for reaction k , listed in **Table S1**. Heat generation from buffer reactions accounts for the enthalpy change of homogeneous reaction n , ΔH_n ,

$$\Omega_B = \sum_n \Delta H_n \left(k_n \prod_{s_{j,n} < 0} c_j^{-s_{j,n}} - \frac{k_n}{K_n} \prod_{s_{j,n} > 0} c_j^{s_{j,n}} \right) \quad (41)$$

and the heat of vaporization for water, ΔH_{vap} , is accounted for in Ω_{PT} ,

$$\Omega_{PT} = -k'_{MT}(100\% - RH) \left[H_0 \left(\frac{p_L}{p^{ref}} \right) + H_0(RH - 100\%) \right] \Delta H_{vap} \quad (42)$$

Joule heating occurs due to both electronic and ionic resistivity

$$\Omega_J = \frac{i_S^2}{\sigma_{S,m}^{eff}} + \frac{i_L^2}{\kappa^{eff}} \quad (43)$$

Model parameters and effective properties

Intrinsic parameter values for the membrane/ionomer and GDE properties are summarized in **Table S2** and **Table S3**. The diffusion coefficient of gaseous species i is a parallel addition of the mass-averaged Stefan-Maxwell diffusivity,

$$D_i^{SM} = \frac{1 - \omega_i}{\sum_{q \neq i} \frac{y_q}{D_{iq}}} \quad (44)$$

and the Knudsen diffusivity,

$$D_i^K = \frac{2r_{pore,m}}{3} \sqrt{\frac{8RT}{\pi M_i}} \quad (45)$$

as

$$D_i = \left(\frac{1}{D_i^{\text{SM}}} + \frac{1}{D_i^{\text{K}}} \right)^{-1} \quad (46)$$

The binary gas-phase diffusion coefficients, D_{iq} , are estimated following derivation by Fuller et al. (Equation S2),⁴⁶ and $r_{\text{pore},m}$ is the average pore radius of medium m . The diffusion coefficient of neutral species are taken from their values in water;⁴⁷ the diffusion coefficient of ionic species in the membrane are derived from the membrane conductivity (Equation S3). The conductivity values reported in **Table S3** are measured for the HCO_3^- -form AEM; we assume the same conductivity value for the CO_3^{2-} -form and the HCOO^- -form AEM, a 10x smaller value for the H-form, and a 5x higher value for the OH-form AEMs.^{15, 48, 49} The effective properties of the membrane/ionomer depend on the fraction of membrane pores equilibrated with liquid water, S_M ,

$$X^{\text{eff},M} = S_M X_L + (1 - S_M) X_V \quad (47)$$

where X_L is the liquid-equilibrated value and X_V is the vapor-equilibrated value listed in **Table S3**. S_M is determined from $p_{L,M}$ as derived by Weber et al.; the relationship between S_M and $p_{L,M}$ is shown in **Figure S2b**.¹⁶

Finally, all properties in the CL and DM domains need to be further corrected for tortuosity and porosity using Bruggeman's correlation,

$$X_m^{\text{eff}} = \epsilon_{p,m}^{1.5} X_m \quad (48)$$

where $\epsilon_{p,m}$ is the volume fraction of the phase of interest, p , in medium m . For example, diffusivity values of ionic species in the CL would be corrected with the volume fraction of ionomer in the CL, $\epsilon_{I,CL}$, whereas diffusivity values of gaseous species in the CL need to be corrected with $\epsilon_{G,CL}$. The volume fractions, $\epsilon_{p,m}$, are calculated from the intrinsic porosity of medium m , ϵ_m^o , the ionomer volume fraction in the pore space, $f_{I,m}$, and the saturation level of medium m , S_m , as

$$\epsilon_{S,m} = 1 - \epsilon_m^o \quad (49)$$

$$\epsilon_{I,m} = \epsilon_m^o f_{I,m} \quad (50)$$

$$\epsilon_{L,m} = \epsilon_m^o (1 - f_{I,m}) S_m \quad (51)$$

$$\epsilon_{G,m} = \epsilon_m^o (1 - f_{I,m}) (1 - S_m) \quad (52)$$

Boundary conditions

The boundary conditions are summarized in **Table 2**. ϕ_S is referenced to the potential at the cathode CH|DM boundary, and set to the applied cell potential at the anode CH|DM boundary. p_G is set to 1 atm at the two gas channels. The boundary condition for p_L at the anode depends on whether the anode feed is humidified gas or liquid water. If it is a liquid feed, $p_L = p_G$ must be satisfied at the CH|DM boundary. If it is a gas feed and $p_L \leq p_G$ at the CH|DM boundary, then a no-flux condition is applied. Pressure inequality is maintained by surface tension in the GDE porous media. Once $p_L > p_G$, there will be an outward flux of liquid water with a mass-transfer coefficient $k'_{MT} = 1 \text{ kg/m}^2\text{s}$ set to an arbitrarily high value to maintain pressure balance of $p_G = p_L$ at the CH|DM boundary.⁵⁰ A fixed mass fraction is assumed at both the anode and cathode CH|DM boundaries, with feed compositions set to 100% RH N_2 and 100% RH CO_2 , respectively. This corresponds to 3 mol% H_2O at 298 K and 43 mol% H_2O at 350 K. The temperature is set to the operating temperature, T_0 , at the two CH|DM boundaries for gas feed conditions.

Table 2 Summary of boundary conditions

	Anode CH DM	Cathode CH DM
ϕ_S	V_{cell}	0 V
p_G	1 atm	
p_L	$\mathbf{n} \cdot \rho_L \mathbf{u}_L = k'_{\text{MT}} \frac{p_L - p_G}{1 \text{ Pa}} \text{step}\left(\frac{p_L - p_G}{1 \text{ Pa}}\right)$ (Gas feed)	
	p_G (Liquid feed)	--
	$\omega_w = \frac{p_w^{\text{vap}} M_w}{p_G M_A}$	$\omega_w = \frac{p_w^{\text{vap}} M_w}{p_G M_A}$
ω_i	$\omega_{\text{N}_2} = 1 - \omega_w$	$\omega_{\text{CO}_2} = 1 - \omega_w$
	$\omega_{i \neq w, \text{N}_2} = 0$	$\omega_{i \neq w, \text{CO}_2} = 0$
T	T_0	

	Anode DM CL	Anode DM CL
ϕ_L	$\nabla \phi_L = 0$	$\nabla \phi_L = 0$
c_j	$\nabla \cdot \mathbf{N}_j = 0$	$\nabla \cdot \mathbf{N}_j = 0$
μ_0	$\nabla \cdot \mathbf{N}_w = 0$	$\nabla \cdot \mathbf{N}_w = 0$

Numerical Method

The governing equations are solved with the COMSOL Multiphysics 5.5 software using the MUMPS solver with a relative tolerance of 0.001. The modelling domain has a maximum element size of 0.1 μm , with element sizes decreased to 10^{-3} μm near each domain boundary to capture sharp concentration gradients.

Results and Discussion

Product distribution and polarization breakdown

The product distribution and the overall simulated polarization curve are shown in **Figure 2a** and **Figure 2b**, respectively. This distribution is what one would expect for a rough Cu surface²¹ operated in an MEA system, if CO₂R kinetics in the CL were identical to those measured in an aqueous electrolyte (specifically CsHCO₃). It is important to note that the rates and product distributions presented here are likely to deviate from those seen in experimental studies of Cu-MEAs because the rate parameters used in our model do not account for the microstructure, catalyst-ionomer interactions, etc. characteristic of the catalyst in the CLs of an MEA. Therefore, we urge the readers to focus on the trends observed as functions of MEA properties and operating conditions – in particular, the impact of water and thermal management, and related mass and charge transport aspects – rather than the extent to which our simulations match specific experimental observations for specific products.

As seen in **Figure 2a**, the product distribution is a strong function of the cell potential. Below about 2.5 V, the principal products are H₂, CO, and HCOOH. CO₂R produces HCOO⁻ but it cannot leave the AEM without converting to HCOOH since it is negatively charged. As the total current density (TCD) increases and OH⁻ anions are produced in the cCL, the equilibrium between HCOOH and HCOO⁻ shifts towards HCOO⁻ in the cCL. Diffusion and migration drive HCOO⁻ to the aCL where the OH⁻ concentration is low due to the OER. Therefore, the fraction of HCOOH collected at the cathode side (depicted by the lighter shade of yellow in **Figure 2a**) decreases with cell potential and TCD. This conclusion is consistent with observations of Gabardo et al.¹³ We note, however, that our simulation neglects formate oxidation at the anode, a process that has been reported and warrants further study.^{13, 51} For cell potentials above 2.5 V, the distribution of products shifts progressively to form C₂H₄, EtOH, and PrOH. These C₂₊ products benefit from the high cathode overpotential in the cCL due to their relatively high transfer coefficient compared to H₂ and C₁ products.

Figure 2b shows both the total polarization curve as well as the applied-voltage breakdown (AVB) of a fully vapor-fed Cu-MEA operated at feed temperature of 298 K. The AVB is calculated using the equations given in **Table S4**. The components of the AVB are categorized as thermodynamic, kinetic, transport, and ohmic, and each of these components is discussed in detail below.

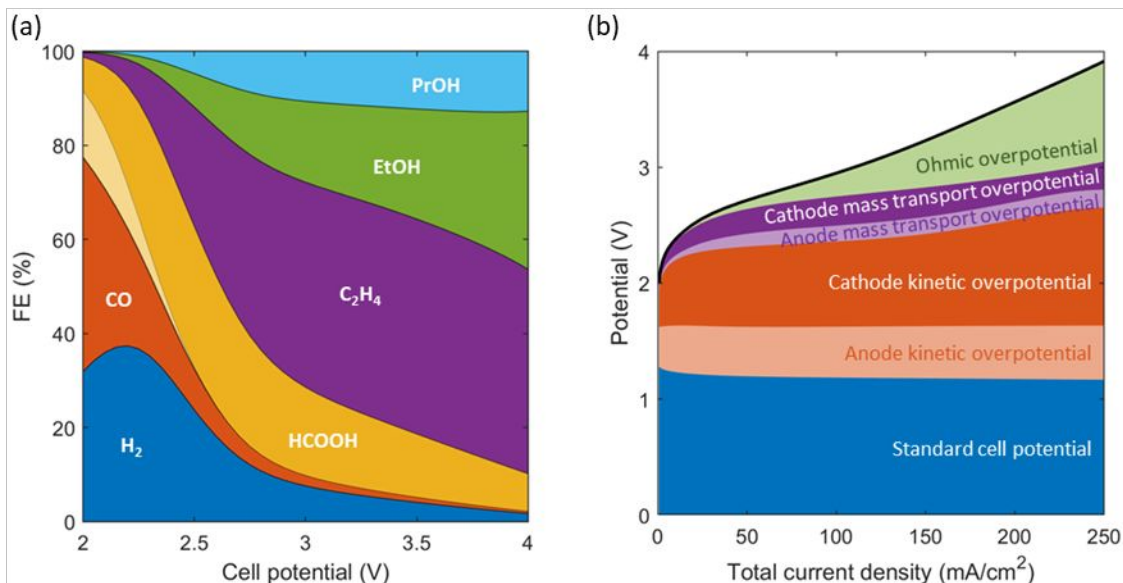


Figure 2 (a) The product distribution and (b) the applied-voltage breakdown (AVB) of the base-case Cu-MEA (100% RH N₂ anode feed and 100% RH CO₂ cathode feed at 298 K). The lighter shade of yellow in (a) represents formic acid collected in the cathode chamber.

Standard cell potential

The standard cell potential is the thermodynamic potential required to drive the reactions at the two electrodes. It varies with the TCD to reflect the changes in the distribution of products formed in the cCL. As the FEs for C₂H₄, EtOH, and PrOH increase, the standard cathode potential, U_{cathode}^0 , increases because of the higher U^0 values of these products, leading to a decrease in the standard cell potential. It is worth mentioning that the standard cell potential can be further decreased by replacing the OER at the IrO₂ anode with another oxidation reaction with a lower standard potential.^{52, 53} For example, a recent study has reported a 0.9 V decrease in cell potential by replacing the IrO₂ anode with Pt black to perform glycerol oxidation.⁵⁴

Kinetic overpotential

The kinetic overpotential drives the charge transfer reactions at the two electrodes and depends on the catalytic activity of the electrode. The simulation shows that increasing cathode loading by increasing cCL thickness, L_{cCL} , or specific surface area, a_s^0 , has little effect on the cell potential for a given TCD above 100 mA/cm² (**Figure 3**). For TCD > 150 mA/cm², a tenfold increase in the specific surface area led to no more than 10% increase in the TCD. Furthermore, we did not see a significant drop in the TCD

until the catalyst loading was decreased by an order of magnitude. These observations suggest that the Cu-MEA is not operating in a kinetically limited regime above 100 mA/cm².

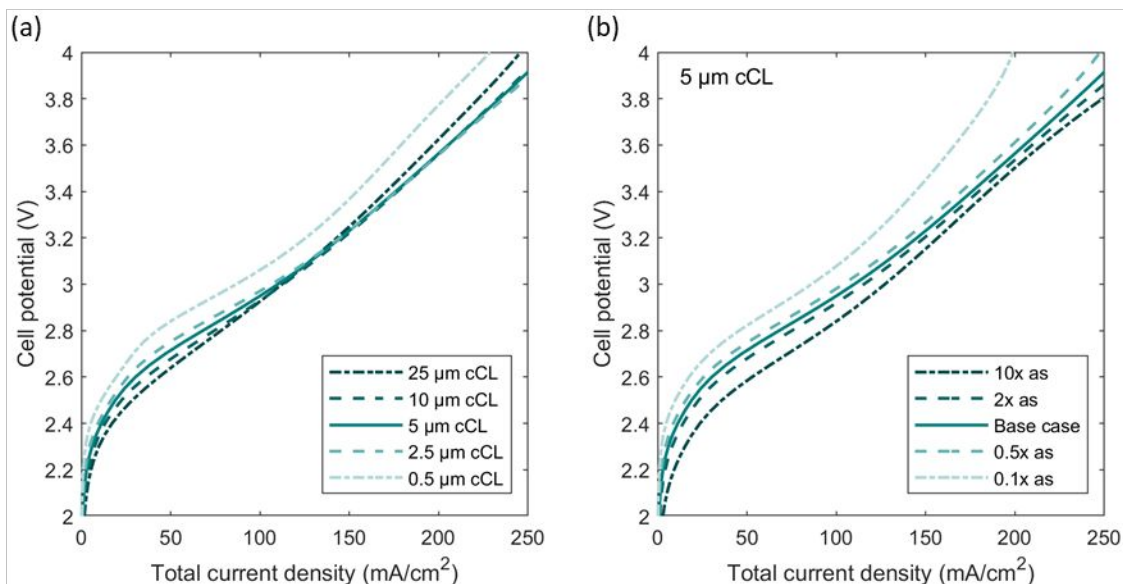


Figure 3 Polarization curves for Cu-MEAs simulated with different (a) cCL thicknesses and (b) specific surface areas. Feed composition: 100% RH N₂ anode feed and 100% RH CO₂ cathode feed at 298 K.

While the polarization curve is relatively insensitive to the properties of the cCL, the product distribution is not, as seen in **Figure 4** and **Figure S3**. Decreasing either the cCL thickness or the specific surface area increases the selectivity to C₂H₄, EtOH, and PrOH. This is because a lower catalyst loading leads to a higher cathode kinetic overpotential (**Figure S4**), which disproportionately promotes the production rates of products with a larger transfer coefficient (see Equation (10)), namely C₂₊ products (**Table 1**). C₂H₄, EtOH, and PrOH have larger transfer coefficients, so their reaction rates increase more with higher overpotentials. These relationships allow one to improve the EE for producing C₂₊ products without significant compromise in the total current density, as shown in **Figure S5**. We also note a tradeoff in the H₂ FE: at low cell potentials, where the system is more kinetically controlled, decreasing the cCL thickness decreases the TCD more significantly, leading to a lower OH⁻ concentration in the cCL, thereby increasing the H₂ FE; at high cell potentials, where the TCD change is smaller, a thinner cCL leads to a higher rate of OH⁻ production per cCL volume via the charge transfer reactions, resulting in a higher OH⁻ concentration in the cCL and lower HER rates. **Figure 4** demonstrates that the thickness of the cCL is a critical parameter for determining the product distribution. The highest FEs for C₂₊ products are achieved with a cCL thickness of 0.5 μm. In this case, the FEs for C₂H₄, EtOH, and PrOH are 48%, 26%, and 15%, respectively, which are reached for a cell potential of 3.2 V and a TCD of 126 mA/cm². Increasing the TCD

from 130 mA/cm² to 230 mA/cm² leads to a modest reduction in the C₂H₄ and PrOH FEs, and a rise in EtOH FE. In other words, the production rate of C₂H₄ and PrOH is not increasing as rapidly as that of EtOH, a result of: (1) the increase in overpotential favors products with a higher transfer coefficient; (2) as CO₂ and H₂O are consumed, products with lower reaction orders are less affected by the decrease in reactant concentration (discussed in the next section). However, since the applied cell potential is also increased, the resulting EEs for C₂₊ products do not improve significantly (**Figure S5**).

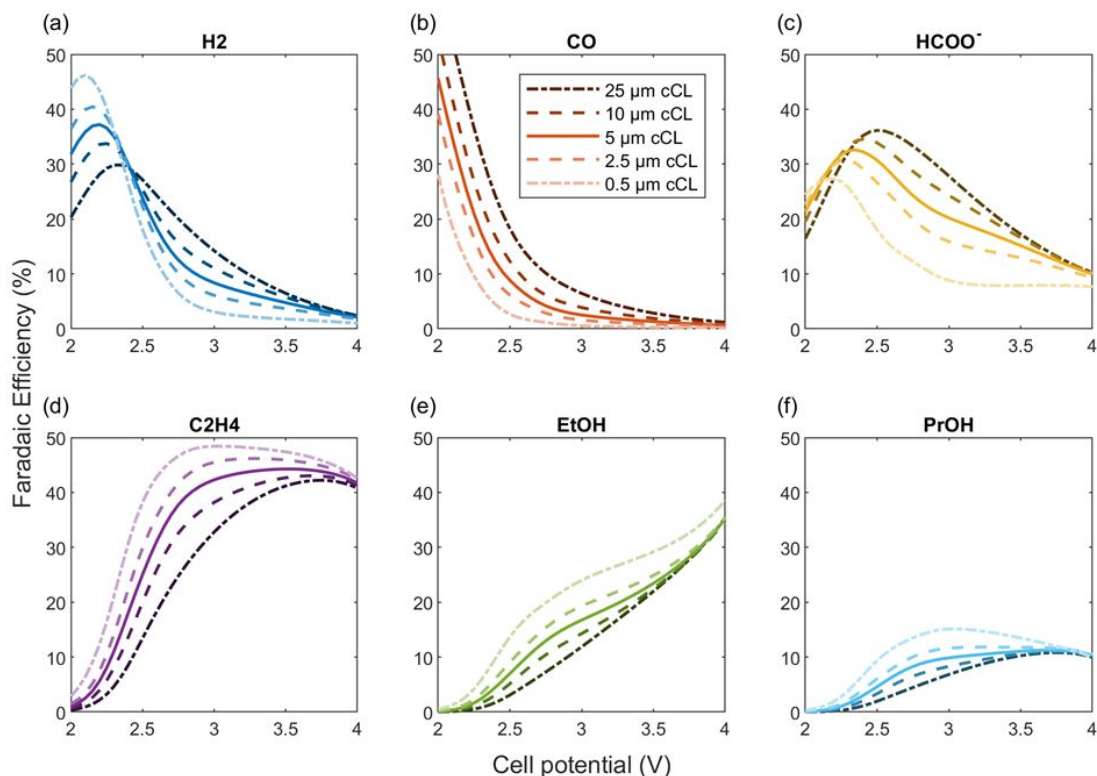


Figure 4 The faradaic efficiencies as a function of the cell potential for the six cathode products for Cu-MEAs with a 25 μm, 5 μm, 2.5 μm, and 0.5 μm cCL. Lighter shade represents a thinner cCL. Feed composition: 100% RH N₂ anode feed and 100% RH CO₂ cathode feed at 298 K.

Changes in the FEs with cCL thickness become less pronounced as the cell potential increases because of the potential gradient that develops in the cCL. **Figure 5a** clearly shows that the cathode potential becomes increasingly non-uniform as the applied cell potential increases, leading to sharp gradients in the local current density shown in **Figure 5b**. At 4 V cell potential, the CL region closer to the membrane is significantly more active – a thinner cCL merely removes the portion of the CL that is barely active, minimally affecting the product distribution and overall cell performance. The CL thickness results discussed here are consistent with experimental results by Dinh et al., who observed little TCD dependence on CL thickness above 100 mA/cm², but higher C₂H₄ FE and lower H₂ FE between 200 and 300

mA/cm^2 with thinner cCLs.⁷ Finally, we note that the anode kinetic overpotential is consistently less than the cathode kinetic overpotential and can be further decreased by using an anode catalyst with improved OER kinetics. **Figure S6** shows that the cell potential can be reduced by roughly 0.2 V at $260 \text{ mA}/\text{cm}^2$ by using an anode catalyst with a 50% larger transfer coefficient for OER. Whereas changes to the anode catalyst do not significantly affect the product distribution at the cathode (**Figure S7**).

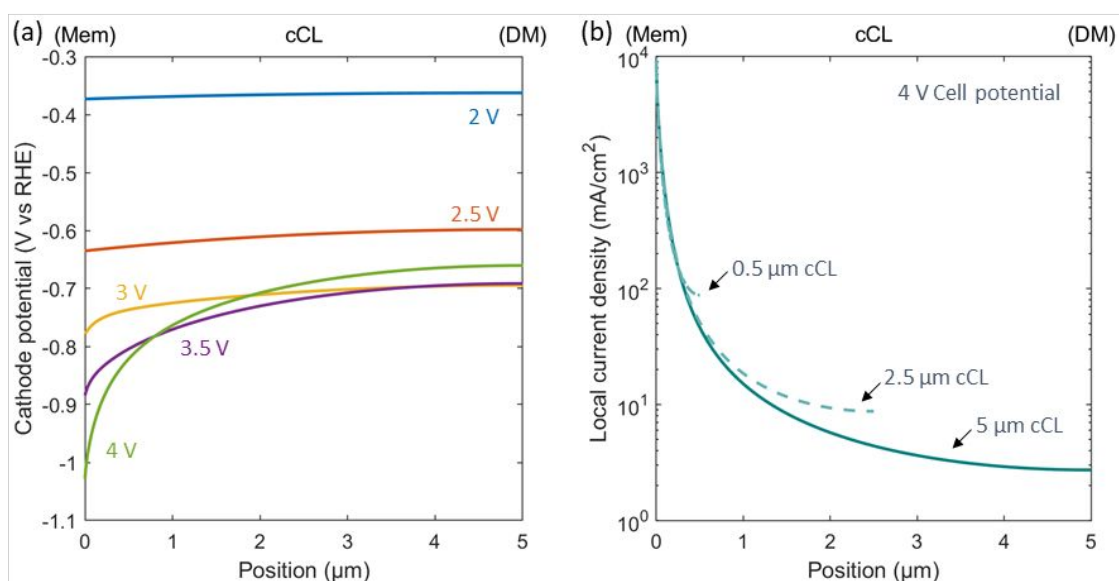


Figure 5 (a) The local cathode potential vs RHE in the $5 \mu\text{m}$ cCL at different cell potentials and (b) the local current-density distribution in the cCL at 4 V cell potential for different cCL thicknesses. The potential gradient developed in the cCL at high cell potentials leads to poor catalyst utilization, where parts of the catalyst close to the membrane (position 0) are much more active than the remaining parts of the cCL. Feed composition: 100% RH N_2 anode feed and 100% RH CO_2 cathode feed at 298 K.

Mass transport and ohmic overpotential

The mass-transport overpotentials in **Figure 2b** mainly arise from deviations in the local OH^- and H_2O concentrations from their initial concentrations, whereas the local CO_2 concentration remains close to saturation in the MEA cCL, as shown in **Figure 6**. This behavior is radically different from what happens in aqueous electrolyte systems where H_2O is abundant (55 M) and the supply of CO_2 becomes mass-transfer limited for TCD $> 10 \text{ mA}/\text{cm}^2$.^{55, 56} This observation points to the importance of understanding the dependence of the CO_2R on the activity of water in order to predict and control the CO_2R selectivity in Cu-MEAs. The lower water activity in the cCL at high cell potentials is caused by the consumption of water by the cathode reactions, the electro-osmotic flux of water towards the anode, and the temperature increase in the membrane and CLs. **Figure 7** shows that for the case where the feed temperature is 298 K, the cell can heat up by up to 3 K at $250 \text{ mA}/\text{cm}^2$ TCD due to the ionic resistivity, heats associated with the reactions,

etc. The temperature does not rise as rapidly when the feed temperature is raised to 350 K because of better membrane hydration and ionic conductivity, as discussed below. The higher temperature in the CLs lowers the gas phase RH and membrane hydration, resulting in a higher cell potential at the same TCD compared to an isothermal system (**Figure S8**). These trends are consistent with water-management results under water-vapor electrolysis.⁵⁷ In addition to affecting cathode reactions, the low water activity also reduces membrane/ionomer conductivity, leading to an increase in the ohmic overpotential shown in **Figure 2b**.

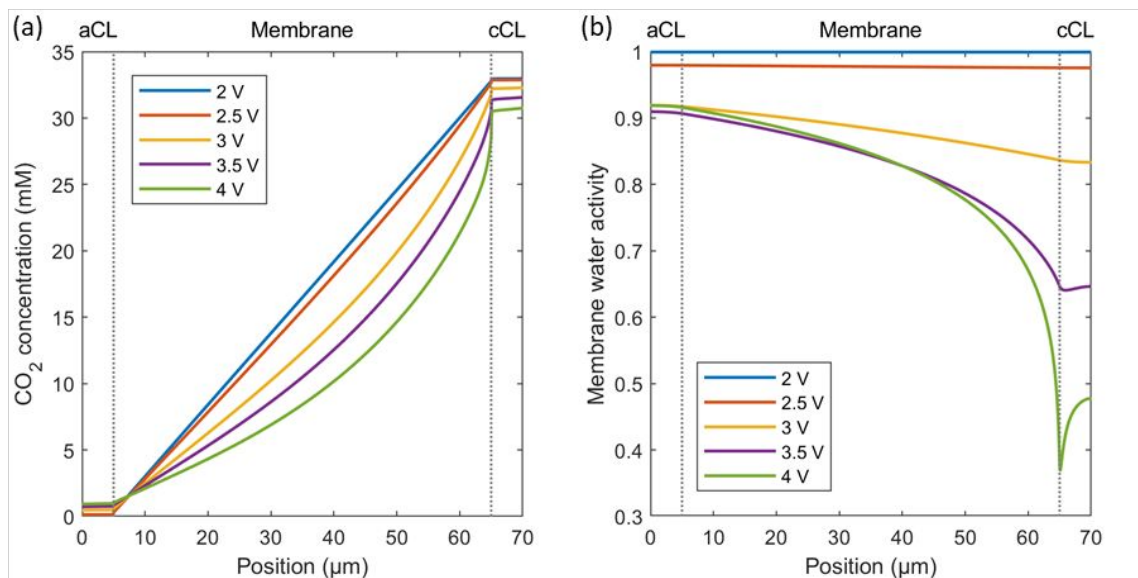


Figure 6 (a) CO₂ concentration and (b) water activity profiles in the ionomer electrolyte at different cell potentials. Unlike aqueous systems, CO₂ concentration remains high near the cathode, whereas H₂O becomes depleted at high current densities. Feed composition: 100% RH N₂ anode feed and 100% RH CO₂ cathode feed at 298 K.

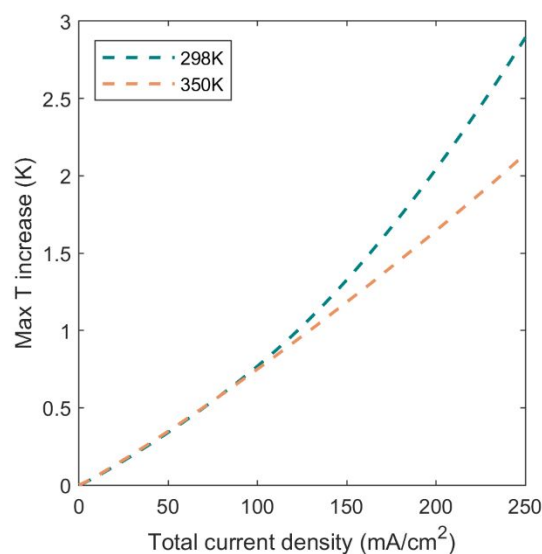


Figure 7 Maximum temperature increase in the Cu-MEA cell operated at 298 K (teal) and 350 K (orange). Feed composition: 100% RH N₂ anode feed and 100% RH CO₂ cathode feed.

Since water supply and management are critical, we performed additional simulations of Cu-MEAs with liquid-water anode feed at 298 K and 350 K, and vapor-water anode feed at 350 K. We also studied the impact of a higher EOC. As expected, feeding liquid water instead of water vapor to the anode increases the attainable TCD at a given cell potential for both operating temperatures, as shown in **Figure 8a**. Comparing the AVBs for the liquid-fed (**Figure 8b**) and vapor-fed (**Figure 2b**) cases, it is clear that the main effect of the liquid-water feed to the anode is to decrease the ohmic overpotential, which is achieved by better hydration of the membrane (**Figure S9a** vs **Figure 6b**). In contrast, liquid-anode feed at 350 K only marginally decreased the cell potential for TCDs up to 250 mA/cm² since the vapor-anode feed at 350 K maintained sufficient membrane hydration at these TCDs (**Figure S9b**). This also highlights that the main effect is water management/hydration and not the temperature dependence of the transport/kinetic properties. Interestingly, the larger EOC has opposite effects on the polarization curve for the vapor-anode and liquid-anode cases. A larger EOC increases the electro-osmotic flux of water from the cathode to the anode at the same TCD, hydrating the aCL but dehydrating the cCL. As the membrane/ionomer conductivity exhibit an exponential dependence on water activity,⁴⁸ this redistribution of water due to the higher EOC improves the overall ionomer electrolyte conductivity for the vapor-anode case. However, since the aCL is already equilibrated with liquid water in the liquid-fed anode case, cCL dehydration has a larger impact on the overall conductivity.

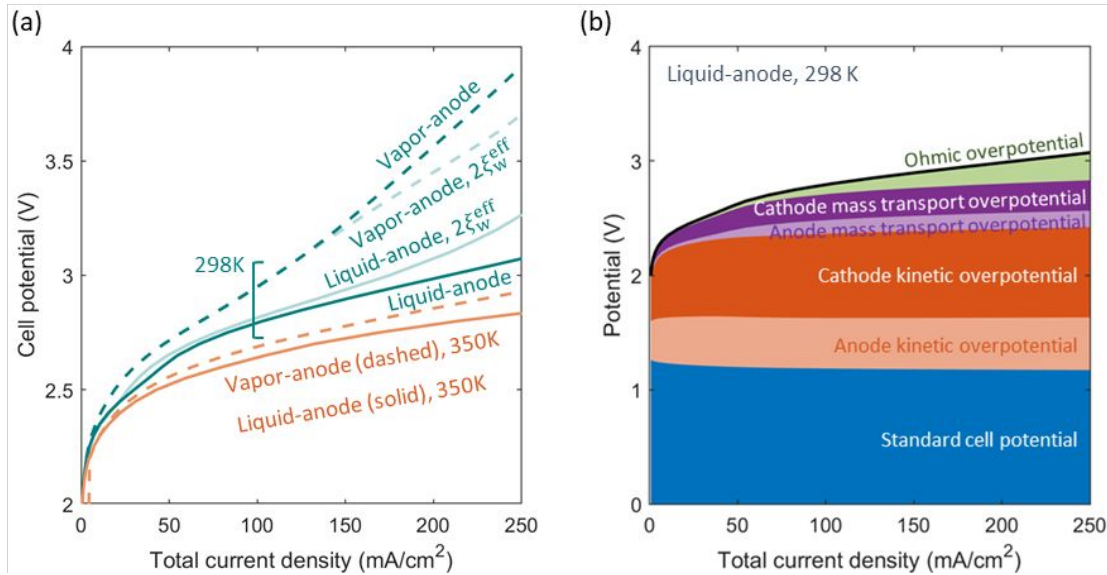


Figure 8 (a) Polarization curves for the vapor-water anode feed (dashed) and liquid-water anode feed (solid) Cu-MEAs at 298 K (teal) and 350 K (orange). Lighter shade represents simulation with 2x EOC. (b) The applied-voltage breakdown (AVB) of the liquid-water anode feed Cu-MEA at 298 K. 100% RH CO₂ is fed to the cathode for all cases.

One challenge with the liquid-fed anode arrangement is that liquid water can readily permeate the membrane and flood the cCL; this occurs at low TCDs (**Figure S10**), and has also been observed experimentally.⁵¹ Cathode flooding blocks CO₂ access to the catalyst in the cCL, resulting in a higher H₂ FE (**Figure 9**).⁶ As the TCD increases, both the rate of water consumption in the cCL and the electro-osmotic flux of water from cathode to anode increases, returning cCL saturation to its irreducible value. We also observe that liquid water is removed from the cCL more rapidly for the membrane with a higher EOC (**Figure S10**). These simulations demonstrate the complexities of water management within these systems and provide guidance for accurate design tradeoffs.

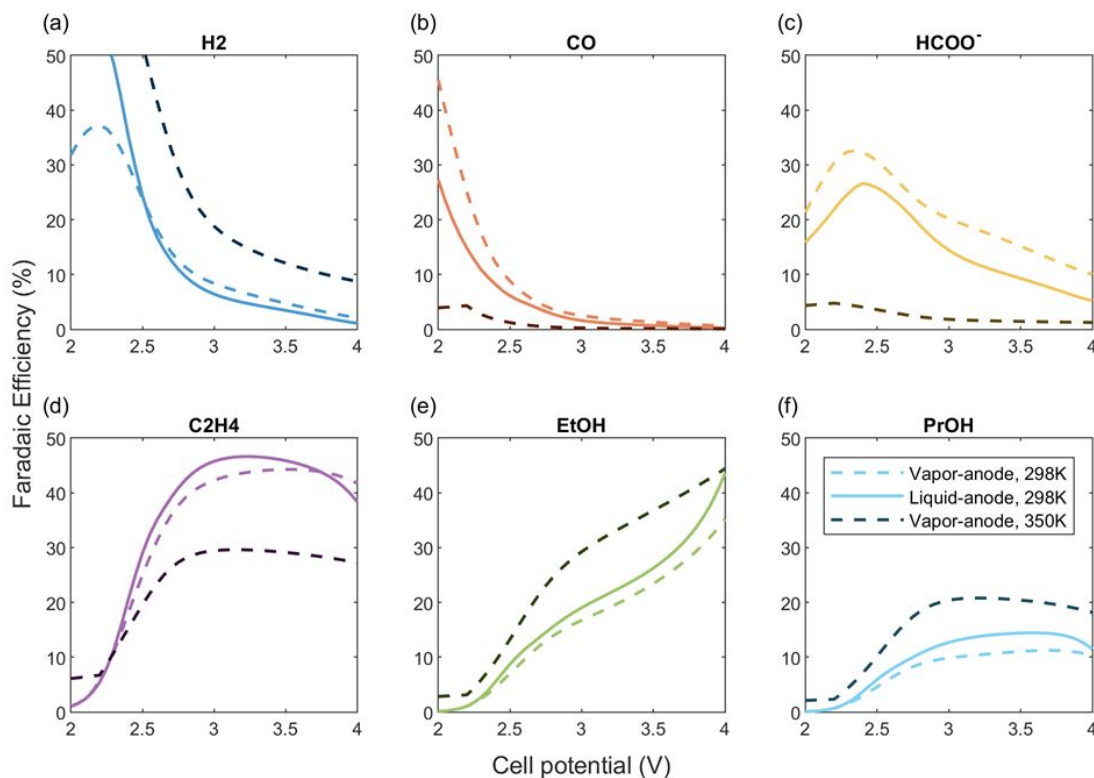


Figure 9 The faradaic efficiencies of the six cathode products for vapor-water anode feed (dashed) and liquid-water anode feed (solid) Cu-MEAs at 298 K (lighter shade) and 350 K (dark gray).

Another way to increase the water supply to the system is to raise the operating temperature. A 100% RH gas stream contains 3 mol% H₂O at 298 K and 43 mol% H₂O at 350 K. A higher temperature also enhances reaction kinetics and improves various transport properties,⁴⁸ but lowers the CO₂ concentration in the supply and its solubility in the membrane.⁵⁸ These temperature dependences are listed in **Table S2**. We examined these tradeoffs by simulating the vapor-fed Cu-MEA at 350 K. An even lower cell potential is required to obtain the same TCD at 350 K than feeding liquid water at 298 K (**Figure 8a**). Increasing the temperature significantly decreases the ohmic and mass-transport overpotentials because of improved membrane hydration and transport properties. Even at a cell potential of 3 V, which corresponds to a TCD of 300 mA/cm², the water activity in the membrane is maintained above 0.85 for the vapor-fed Cu-MEA at 350 K (**Figure S9b**). As a result of both the increased temperature and hydration, the membrane maintains a higher conductivity, and therefore, a lower ohmic overpotential at 350 K. Higher membrane conductivity also means higher diffusivities for the ionic species, resulting in a smaller OH⁻ concentration gradient across the cell, thereby decreasing the mass-transport overpotential.

The improved transport properties at 350 K also lead to a lower OH⁻ concentration in the cCL, and a higher H₂ FE (**Figure 9a**). The observed changes in the FEs for CO₂R products are due to multiple factors:

(1) CO_2 solubility in the ionomer decreases with increasing temperature, as does the concentration of CO_2 in the humidified cathode gas feed as noted above. Products with a higher reaction order with respect to CO_2 will be more sensitive to this decrease in CO_2 concentration and exhibit a lower FE. (2) Products with a higher activation energy (i.e. C_2H_4 , EtOH, PrOH) are more sensitive to an increase in the operating temperature. (3) Increasing membrane hydration with increasing temperature leads to changes in the cathode overpotential at the same cell potential (**Figure S11**); a higher cathode overpotential benefits products with a higher transfer coefficient, as discussed above. Overall, increasing the temperature enhances the selectivities to EtOH and PrOH because of their relatively lower reaction order with respect to CO_2 , higher activation energy, and higher transfer coefficient compared to the other cathode products. On the other hand, the increase in the production rates of CO, HCOO^- , and C_2H_4 at 350 K is not as significant compared to EtOH and PrOH, so we observe a drop in their FEs. The higher H_2 FE and lower C_2H_4 FE at 350 K agrees qualitatively with experimental work reported by Gabardo et al. reported for a Cu-MEA.¹³

Generalizing the findings

As mentioned above, a single set of self-consistent kinetics derived from aqueous experiments was used in all the above simulations. To demonstrate that the findings are general, we performed simulations using a second set of experimentally derived kinetics, knowing that a complete set of kinetics in MEA environments with Cu nanoparticles remain elusive. Furthermore, to demonstrate the impact of moving from an aqueous system to an MEA architecture, the differences between the FEs obtained from simulation of the Cu-MEA and the aqueous analog for both sets of kinetics (a rough Cu surface operated in 0.1 M CsHCO_3 and a polished Cu surface operated in 0.1 M KHCO_3) are given in **Figure 10**. This comparison at different cathode potentials allows one to generalize the above findings and help deconvolute the specific kinetics with the influence of the MEA architecture. The cathode potential for the MEA system is chosen to be the potential at the membrane|cCL interface, where the catalyst is most active (**Figure 5**). It is important to note that the potential gradient in the cCL also affects the overall product distribution and contributes to the changes observed in **Figure 10**. We observe that the MEA architecture suppresses the formation of H_2 and CO and promotes the formation of C_{2+} products, irrespective of which set of kinetics is used. These trends are a consequence of the higher OH^- and CO_2 concentrations in the cCL and consistent for both sets of kinetic parameters. Interestingly, the second set of kinetics shows that the MEA promotes a greater shift towards EtOH with a stronger dependence on applied potential compared to first set, a result of the larger EtOH transfer coefficient from the kinetics II

(Table S5). The analysis emphasizes the need to characterize CO₂R catalysts under vapor-fed conditions and better understand the impacts of the different local environments created by the ionomer electrolyte.

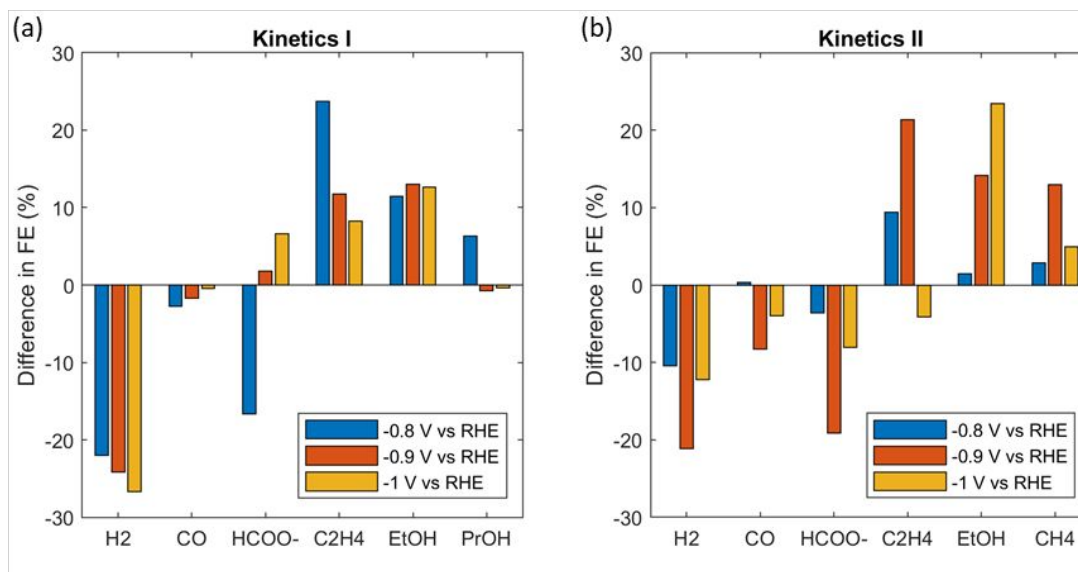


Figure 10 The percentage point difference in the FEs predicted for the vapor-fed Cu-MEA and the experimentally measured FEs. The Cu-MEA was simulated with rate parameters extracted from two sets of experimental results derived from (a) reference 21 (Table 1), and (b) reference³⁰ (Table S5). The cathode potential for the MEA system is taken to be the potential at the membrane|cCL interface.

Conclusions

We have developed a multiphysics model to study the performance and limitations of CO₂R on Cu in an MEA configuration. We observed that the cCL thickness and specific surface area have a much smaller impact on the TCD than the product distribution at a given cell potential, indicating that the Cu-MEA is not kinetically limited between 100~250 mA/cm². Decreasing catalyst loading shifts the selectivity towards C₂₊ products products with larger transfer coefficients. This effect is less pronounced at high cell potentials because of the sharp gradient in potential that develops in the cCL at high TCDs, an effect that limits catalyst utilization. Examination of the voltage losses due to mass-transport and membrane resistance reveals that Cu-MEAs suffer from limitation in anion transport through the ionomer and membrane caused by inadequate hydration. These limitations can be overcome by feeding liquid water to the anode or increasing the operating temperature for a fully-vapor system. Liquid water readily hydrates the membrane but can lead to flooding of the cCL at low current densities, thereby causing poor mass transport of CO₂ to the catalyst in the cCL.^{6, 51} Increasing the operating temperature increases ionomer hydration as well as the rates of products with higher activation energies (e.g., C₂H₄, EtOH, PrOH).

However, a higher temperature results in a lower CO_2 concentration in the ionomer (due to both the higher mole fraction of inlet H_2O vapor and a lower CO_2 solubility). These tradeoffs eventually benefit products with a higher activation energy and a lower reaction order with respect to CO_2 at higher temperatures. Overall, a vapor-water anode feed is advantageous in avoiding cathode flooding and salt precipitation issues seen in CO_2R electrolyzers.^{7, 10, 51, 59} A fully-vapor system is also beneficial for photo-electrochemical systems in avoiding light-scattering caused by bubble formation.⁶⁰⁻⁶² However, for sufficient water supply, a fully vapor-fed CO_2R electrolyzer must be operated at elevated temperatures. This work emphasizes the critical role of ionomer and membrane hydration on the performance and distribution of products formed by CO_2R .

Finally, we note that the kinetics used in our simulations based on those observed for CO_2R in an aqueous solution of CsHCO_3 , and hence, do not account for the specific microenvironment effects on the Cu kinetics related to the ionomer surrounding the Cu nanoparticles in the CL. Since we show that the intrinsic rate parameter for CO_2R are important for defining the product distribution, further work is needed to define the influence of the ionomer on these parameters and to measure them experimentally for an MEA CL. Notwithstanding this limitation, the present simulations are highly informative and demonstrate how the properties of a Cu-MEA and its mode of operation impact the utilization of the applied voltage for promoting CO_2R .

Acknowledgements

This material is based upon work performed by the Joint Center for Artificial Photosynthesis, a DOE Energy Innovation Hub, supported through the Office of Science of the U.S. Department of Energy under Award Number DE-SC0004993.

List of Symbols

Roman

a_s	specific surface area, m^{-1}
a_j	activity of species j
c_j	concentration of species j , mol m^{-3}
D_i	diffusivity of species i , $\text{m}^2 \text{s}^{-1}$
F	Faraday's constant, C mol^{-1}
H_i	Henry's constant of species i , M atm^{-1}
i	electrolyte current density, mA cm^{-2}
i_o	exchange current density, mA cm^{-2}
i_S	electrode current density, mA cm^{-2}
j_i	diffusive mass flux of species i , $\text{g m}^{-2} \text{s}^{-1}$
k_{MT}	mass transfer coefficient, m s^{-1}
k_n	rate constant for homogeneous reaction n , s^{-1}
K_n	equilibrium constant for homogeneous reaction n
M_i	molar mass of species i , g mol^{-1}
n_i	mass flux of species i , $\text{g m}^{-2} \text{s}^{-1}$
n_k	number of electrons transferred in reaction k
N_j	molar flux of species j , $\text{mol m}^{-2} \text{s}^{-1}$
p	pressure, atm
Q	volumetric mass source, g m^{-3}
$r_{p,m}$	pore radius in medium m ,
R	gas constant, $\text{J mol}^{-1} \text{K}^{-1}$
R_i	volumetric molar source terms for species i , $\text{mol m}^{-3} \text{s}^{-1}$
$S_{i,k}$	stoichiometric coefficient of species i in reaction k
S_m	saturation of medium m
ΔS_n	change of entropy for reaction n , $\text{J mol}^{-1} \text{K}^{-1}$
T	temperature, K
u	mass-averaged fluid velocity, m s^{-1}
U_k^o	reference potential of reaction k , V
$v_{p,i}$	diffusion volume of species i
V_i	molar volume of species i , ml mol^{-1}
x_j	mole fraction of aqueous species j
y_i	mole fraction of gaseous species i
z_i	charge of species i

Greek

$\alpha_{a/c,k}$	anodic/cathodic transfer coefficient of reaction k
α_0	water transport coefficient, $\text{mol}^2 \text{J}^{-1} \text{cm}^{-1} \text{s}^{-1}$
$\gamma_{j,k}$	reaction order with respect to species j for reaction k
$\epsilon_{p,m}$	volume fraction of phase p in medium m

ϵ_m^o	intrinsic porosity of medium m
η_k	surface overpotential for reaction k , V
κ	electrolyte conductivity, S m ⁻¹
λ	water content
μ_0	water chemical potential, J mol ⁻¹
ξ	electro-osmotic coefficient
ρ	mass density, g cm ⁻³
σ_S	electronic conductivity, S m ⁻¹
ϕ_L	electrolyte potential, V
ϕ_S	electronic potential, V
ψ	permeability, m ²
ω_i	mass fraction of species i
Ω	volumetric heat source, W/m ³

Subscript

a	anodic
c	cathodic
i	gaseous species
j	species in the ionomer
k	charge transfer reaction
m	medium: DM, CL, Mem, Ion,
n	homogeneous reaction
p	phase
A	average
B	bulk homogeneous
CT	charge transfer
G	gas phase
L	liquid phase
M	membrane
MT	mass transfer
PT	phase transfer
S	solid phase
V	water vapor
α	transfer coefficient
0	water

Superscript

eff	effective property
eq	equilibrium
K	Knudsen
o	standard condition
ref	reference state

sat	saturation
SM	Stefan-Maxwell
M	membrane

References

1. O. S. Bushuyev, P. De Luna, C. T. Dinh, L. Tao, G. Saur, J. van de Lagemaat, S. O. Kelley and E. H. Sargent, *Joule*, 2018, **2**, 825-832.
2. J. W. Ager and A. A. Lapkin, *Science*, 2018, **360**, 707-708.
3. S. Verma, B. Kim, H. R. Jhong, S. Ma and P. J. Kenis, *ChemSusChem*, 2016, **9**, 1972-1979.
4. S. Verma, X. Lu, S. Ma, R. I. Masel and P. J. Kenis, *Phys. Chem. Chem. Phys.*, 2016, **18**, 7075-7084.
5. K. Hara, N. Sonoyama and T. Sakata, *Stud. Surf. Sci. Catal.*, 1998, **114**, 577-580.
6. L. C. Weng, A. T. Bell and A. Z. Weber, *Phys. Chem. Chem. Phys.*, 2018, **20**, 16973-16984.
7. C. T. Dinh, T. Burdyny, M. G. Kibria, A. Seifitokaldani, C. M. Gabardo, F. P. G. de Arquer, A. Kiani, J. P. Edwards, P. De Luna, O. S. Bushuyev, C. Q. Zou, R. Quintero-Bermudez, Y. J. Pang, D. Sinton and E. H. Sargent, *Science*, 2018, **360**, 783-787.
8. D. S. Ripatti, T. R. Veltman and M. W. Kanan, *Joule*, 2019, **3**, 240-256.
9. I. Sullivan, L. Han, S. H. Lee, M. Lin, D. M. Larson, W. S. Drisdell and C. Xiang, *ACS Sustainable Chemistry & Engineering*, 2019, **7**, 16964-16970.
10. M. Jouny, W. Luc and F. Jiao, *Nature Catalysis*, 2018, **1**, 748-755.
11. L. C. Weng, A. T. Bell and A. Z. Weber, *Energy Environ. Sci.*, 2019, **12**, 1950-1968.
12. R. L. Cook, R. C. Macduff and A. F. Sammells, *J. Electrochem. Soc.*, 1988, **135**, 1470-1471.
13. C. M. Gabardo, C. P. O'Brien, J. P. Edwards, C. McCallum, Y. Xu, C. T. Dinh, J. Li, E. H. Sargent and D. Sinton, *Joule*, 2019, **3**, 2777-2791.
14. A. Z. Weber and J. Newman, *J. Electrochem. Soc.*, 2004, **151**, A326-A339.
15. M. R. Gerhardt, L. M. Pant and A. Z. Weber, *J. Electrochem. Soc.*, 2019, **166**, F3180-F3192.
16. A. Z. Weber and J. Newman, *J. Electrochem. Soc.*, 2004, **151**, A311-A325.
17. V. J. Bharath, J. Millichamp, T. P. Neville, T. J. Mason, P. R. Shearing, R. J. C. Brown, G. Manos and D. J. L. Brett, *J. Membrane Sci.*, 2016, **497**, 229-238.
18. A. Kusoglu, T. J. Dursch and A. Z. Weber, *Adv Funct Mater*, 2016, **26**, 4961-4975.
19. M. Tesfaye, D. I. Kushner, B. D. McCloskey, A. Z. Weber and A. Kusoglu, *Acs Macro Lett*, 2018, **7**, 1237-1242.
20. P. J. Dudenias and A. Kusoglu, *Macromolecules*, 2019, **52**, 7779-7785.
21. M. Ebaid, K. Jiang, Z. Zhang, W. S. Drisdell, A. T. Bell and J. K. Cooper, *Chem. Mater.*, 2020, DOI: 10.1021/acs.chemmater.0c00761.
22. H. Hashiba, L. C. Weng, Y. K. Chen, H. K. Sato, S. Yotsuhashi, C. X. Xiang and A. Z. Weber, *J. Phys. Chem. C*, 2018, **122**, 3719-3726.
23. J. Resasco, L. D. Chen, E. Clark, C. Tsai, C. Hahn, T. F. Jaramillo, K. Chan and A. T. Bell, *J. Am. Chem. Soc.*, 2017, **139**, 11277-11287.
24. S. Ringe, E. L. Clark, J. Resasco, A. Walton, B. Seger, A. T. Bell and K. Chan, *Energy Environ. Sci.*, 2019, **12**, 3001-3014.
25. H. A. Gasteiger, J. E. Panels and S. G. Yan, *J. Power Sources*, 2004, **127**, 162-171.

26. T. Schuler, A. Chowdhury, A. T. Freiberg, B. Sneed, F. B. Spingler, M. C. Tucker, K. L. More, C. J. Radke and A. Z. Weber, *J. Electrochem. Soc.*, 2019, **166**, F3020-F3031.
27. K. Jiang, Y. Huang, G. Zeng, F. M. Toma, W. A. Goddard and A. T. Bell, *ACS Energy Lett.*, 2020, DOI: 10.1021/acseenergylett.0c00482, 1206-1214.
28. A. Verdaguer-Casadevall, C. W. Li, T. P. Johansson, S. B. Scott, J. T. McKeown, M. Kumar, I. E. L. Stephens, M. W. Kanan and I. Chorkendorff, *J. Am. Chem. Soc.*, 2015, **137**, 9808-9811.
29. Y. Huang, Y. Chen, T. Cheng, L.-W. Wang and W. A. Goddard, *ACS Energy Lett.*, 2018, **3**, 2983-2988.
30. K. P. Kuhl, E. R. Cave, D. N. Abram and T. F. Jaramillo, *Energy Environ. Sci.*, 2012, **5**, 7050-7059.
31. E. Nurlaela, T. Shinagawa, M. Qureshi, D. S. Dhawale and K. Takanabe, *ACS Catal.*, 2016, **6**, 1713-1722.
32. L. Giordano, B. Han, M. Risch, W. T. Hong, R. R. Rao, K. A. Stoerzinger and Y. Shao-Horn, *Catal. Today*, 2016, **262**, 2-10.
33. D. Y. Kuo, J. K. Kawasaki, J. N. Nelson, J. Kloppenburg, G. Hautier, K. M. Shen, D. G. Schlom and J. Suntivich, *J. Am. Chem. Soc.*, 2017, **139**, 3473-3479.
34. T. Schuler, T. Kimura, T. J. Schmidt and F. N. Büchi, *Energy Environ. Sci.*, 2020, DOI: 10.1039/D0EE00673D.
35. L. Wang, S. A. Nitopi, E. Bertheussen, M. Orazov, C. G. Morales-Guio, X. Liu, D. C. Higgins, K. Chan, J. K. Nørskov, C. Hahn and T. F. Jaramillo, *ACS Catal.*, 2018, **8**, 7445-7454.
36. M. Mukaddam, E. Litwiller and I. Pinnau, *Macromolecules*, 2016, **49**, 280-286.
37. V. A. Sethuraman, S. Khan, J. S. Jur, A. T. Haug and J. W. Weidner, *Electrochim. Acta*, 2009, **54**, 6850-6860.
38. E. Wilhelm, R. Battino and R. J. Wilcock, *Chem. Rev.*, 1977, **77**, 219-262.
39. M. Soniat and F. A. Houle, *J. Phys. Chem. B*, 2018, **122**, 8255-8268.
40. D. T. Hallinan and Y. A. Elabd, *J. Phys. Chem. B*, 2007, **111**, 13221-13230.
41. Q. Zhao, N. Carro, H. Y. Ryu and J. Benziger, *Polymer*, 2012, **53**, 1267-1276.
42. N. Ziv, W. E. Mustain and D. R. Dekel, *ChemSusChem*, 2018, **11**, 1136-1150.
43. A. R. Crothers, R. M. Darling, A. Kusoglu, C. J. Radke and A. Z. Weber, *J. Electrochem. Soc.*, 2020, **167**, 013547.
44. A. R. Crothers, R. M. Darling, A. Kusoglu, C. J. Radke and A. Z. Weber, *J. Electrochem. Soc.*, 2020, **167**, 013548.
45. Y. S. Li, T. S. Zhao and W. W. Yang, *Int. J. Hydrogen Energy*, 2010, **35**, 5656-5665.
46. E. N. Fuller, P. D. Schettle and J. C. Giddings, *Ind. Eng. Chem.*, 1966, **58**, 19-+.
47. *CRC handbook of chemistry and physics*, CRC Press, Cleveland, Ohio, 1977.
48. J. Peng, A. L. Roy, S. G. Greenbaum and T. A. Zawodzinski, *J. Power Sources*, 2018, **380**, 64-75.
49. M. R. Singh, E. L. Clark and A. T. Bell, *Phys. Chem. Chem. Phys.*, 2015, **17**, 18924-18936.
50. I. V. Zenyuk, P. K. Das and A. Z. Weber, *J. Electrochem. Soc.*, 2016, **163**, F691-F703.
51. G. O. Larrazábal, P. Strøm-Hansen, J. P. Heli, K. Zeiter, K. T. Therkildsen, I. Chorkendorff and B. Seger, *ACS Appl. Mater. Interfaces*, 2019, **11**, 41281-41288.
52. M. Bevilacqua, J. Filippi, A. Lavacchi, A. Marchionni, H. A. Miller, W. Oberhauser, E. Vesselli and F. Vizza, *Energy Technol.*, 2014, **2**, 522-525.
53. T. Li, Y. Cao, J. He and C. P. Berlinguette, *ACS Central Science*, 2017, **3**, 778-783.
54. S. Verma, S. Lu and P. J. A. Kenis, *Nat Energy*, 2019, **4**, 466-474.
55. N. Gupta, M. Gattrell and B. MacDougall, *J. Appl. Electrochem.*, 2006, **36**, 161-172.
56. E. L. Clark and A. T. Bell, *J. Am. Chem. Soc.*, 2018, **140**, 7012-7020.
57. J. C. Fornaciari, M. R. Gerhardt, J. Zhou, Y. N. Regmi, N. Danilovic, A. T. Bell and A. Z. Weber, *J. Electrochem. Soc.*, 2020, **167**, 104508.
58. X. M. Ren, T. D. Myles, K. N. Grew and W. K. S. Chiu, *J. Electrochem. Soc.*, 2015, **162**, F1221-F1230.

59. M. E. Leonard, L. E. Clarke, A. Forner-Cuenca, S. M. Brown and F. R. Brushett, *ChemSusChem*, 2020, **13**, 400-411.
60. J. M. Spurgeon and N. S. Lewis, *Energy Environ. Sci.*, 2011, **4**.
61. T. A. Kistler, D. Larson, K. Walczak, P. Agbo, I. D. Sharp, A. Z. Weber and N. Danilovic, *J. Electrochem. Soc.*, 2018, **166**, H3020-H3028.
62. P. K. Giesbrecht, A. M. Müller, C. G. Read, S. Holdcroft, N. S. Lewis and M. S. Freund, *Sustainable Energy & Fuels*, 2019, **3**, 3611-3626.